A Multifunctional Biodegradable Prussian blue Analogue for Synergetic Photothermal/Photodynamic/Chemodynamic therapy and Intrinsic Tumor Metastasis Inhibition

Yuting Hao
Southern Medical University
Lianzhi Mao
southern medical university
Rongjun Zhang
Southern Medical University
Xiaoshan Liao
southern medical university
Miaomiao Yuan
Sun Yat-Sen University
Wenzhen Liao (wenzhenliao@163.com)
Southern Medical University

Research

Keywords: Prussian blue analogues, photothermal therapy, photodynamic therapy, chemodynamic therapy, ferroptosis, anti metastasis

Posted Date: February 23rd, 2021

DOI: https://doi.org/10.21203/rs.3.rs-240564/v1

Abstract

Background

To date, various Prussian blue analogues (PBA) have been prepared for biomedical applications due to their unique structural advantages. However, the safety and effectiveness of tumor treatment still need further exploration.

Results

This contribution reports a facile synthesis of novel PBA with superior tumor synergetic therapy effects and a detailed mechanistic evaluation of their intrinsic tumor metastasis inhibition activity. The as-synthesized PBA have a uniform cube structure with a diameter of approximately 220 nm and showed high near infrared light (NIR) photoreactivity, photothermal conversion efficiency (41.44%) and photodynamic effect. Additionally, PBA could lead to chemodynamic effect which caused by Fenton reaction and ferroptosis. The combined therapy strategy of PBA exhibit notable tumor ablation properties due to photothermal therapy (PTT)/photodynamic therapy (PDT)/ chemodynamic therapy (CDT) effect without obvious toxicity *in vivo*. The PBA also demonstrate potential as a contrast agent for magnetic resonance imaging (MRI) and photoacoustic (PA) imaging. More importantly, careful investigations reveal that PBA displays excellent biodegradation and anti-metastasis properties. Further exploration of this PBA implies that its underlying mechanism of intrinsic tumor metastasis inhibition activity can be attributed to modulation of epithelial mesenchymal transition (EMT) expression.

Conclusions

The considerable potential exhibits by as-synthesized PBA make it an ideal candidate as a synergetic therapeutic agent for tumor treatment.

1. Introduction

Recently, nanotechnology as a new strategy for cancer diagnosis and treatment has received much attention in biomedical science.[1–3] PTT, a cancer treatment developed from the application of nanotechnology, is based on the conversion of NIR radiation to induce hyperthermia and then “burn” cancer cells.[4–9] Due to its convenient operation, minimal side effects and noninvasivity, PTT has been considered an alternative approach for clinical usage.[10] However, the therapeutic effect is limited by the use of a single treatment at a safe dosage, uneven distribution of photothermal agents and endothermic effect of blood vessels around tumors also affect the ablation efficacy.[11] Therefore, the combined therapy strategies, such as PTT/PDT, PTT/CDT and PDT/CDT have been proposed and achieved good performance. [12–14] PDT is another type of phototherapy for tumors and is characterized by reactive oxygen species (ROS) generation in tumor environment to kill cancer cells.[15] In addition, PDT can also

decrease tumor nutrition by destroying nearby blood vessels.[16] Another therapy strategy based on ROS generation is called as CDT, which is depedent on Fenton reaction under ferrous ion or transition metal ion.[17] Since the high H_2O_2 content (100 μM to 1 mM) in tumor microenvironment, Fenton reaction can transfer H_2O_2 to toxicant ROS (·OH) and generate O_2 at the same time under ferrous ion catalysis.[13] Thus, CDT process can produce O_2 for PDT while near infrared light irradiation ameliorate ·OH generation in Fenton reaction, which can improve cancer therapeutic efficacy. [17, 18]

To achieve better PTT/PDT/CDT therapeutic efficiency, the preparation of photothermal agent and photosensitizer (PS) which can trigger Fenton reaction or Fenton-like Reaction is critical. To date, some NIR-responsive materials have been developed for photothermal therapy or combined therapy strategies in tumor treatment.[19–22] However, potential safety issues for nanomaterial application always exist concomitantly, and the main contradiction is particle toxicity caused by low biodegradability *in vivo*.[23, 24] The high photothermal conversion efficiency of nanomaterials leads to good PTT performance, but because long-term toxicological evaluations are still scarce, the application of nanomaterials for clinical transformation is limited.[10, 25] Therefore, it is meaningful to synthesize nanomaterials for PTT/PDT/CDT therapy strategies from old substances that have been approved for clinical applications.

Prussian blue (PB) has been used as an ancient dark blue pigment since 1704, and because it is porous and easy to chelate with heavy metals, it has been developed as a drug named “Radiogardase” and approved by the U.S. Food and Drug Administration (FDA) for internal contamination treatment.[26–28] PB has the general formula of $Fe_4^{III}[Fe^{II}(CN)_6]_3 \cdot nH_2O$, consisting of Fe^{II}-CN-Fe^{III} units, and the special properties of PB such as photothermal, photomagnetic and electrochemical characteristics are all attributed to the charge transfer between Fe^{II} and Fe^{III}.[8, 28] Additionally, the excellent biocompatibility, low cost and easy manufacture characteristics of PB attract continued research by scientists. Furthermore, Prussian blue-type nanoparticles, also called PBA, were obtained. PBA are defined by a structure similar to that of PB in which Fe^{III} or $[Fe^{II}(CN)_6]^{4-}$ is replaced by another transition metal.[2, 8] After that, PBA with different shapes, sizes and characteristics have been synthetized for biomedical, photomagnetic, photochemistry, decontamination and other applications.[29–31] Notably, PBA performs well in NIR response and photoreaction, making it as a great candidate for diagnosis or PTT/PDT/CDT therapy for tumors.

Currently, despite the diversity of cancer treatment methods, tumor metastasis is still the greatest problem in cancer therapy.[32, 33] The development of nanotechnology shows great potential for preventing cancer metastasis.[34, 35] In detail, nanoparticles carrying drugs or nanoparticle-based immunotherapy has been reported, both of which have anti-metastasis effects for tumor therapy.[36–38] Additionally, a new method combining PTT and advanced imaging techniques has also been developed as a potential choice for anti-metastasis therapy, and the mechanism involves hyperthermia to burn lymph nodes that have been invaded by cancer cells.[39] However, among the nanoparticle applications in these anti-metastatic strategies, nanoparticles are more commonly used as vehicles or in indirect steps. In contrast, Thao et al. reported that zinc sulfide nanoparticles had the ability to inhibit tumor cell migration and

metastasis with no effect on cell proliferation capacity.[40] Therefore, it should be meaningful to discover nanomaterials which have excellent biocompatibility and anti-metastasis properties for tumor therapy.

Hence, in this study, a novel PBA nanoparticle is synthesized via a facile protocol under mild conditions.[41] According to previous reports, the prepared PBA is expected to be sensitive to NIR radiation and could be an outstanding candidate for PTT/PDT/CDT strategies. Excitingly, at least in nanomaterial applications, the anti-metastatic properties and biodegradation potential of this PBA for tumor therapy are unique (Scheme 1).

2. Results And Discussion

2.1 Synthesis and characterization of PBA

The synthesis of the PBA was based on a precipitation method with slight modification,[41] and compared with the reported studies, all the required materials and steps in this study were simpler and more facile.[2, 42] SEM and TEM images showed that the prepared PBA has a uniform cube structure with a diameter of approximately 220 nm (Fig. 1A-B). Moreover, Fig. 1B also showed that PBA nanoparticles were hollow and could thus be used as drug carriers. Figure 1C displayed a clear lattice structure of PBA recorded by TEM, which demonstrated that PBA had good crystallinity. Additionally, the crystalline structure of PBA was further detected by XRD, and the diffraction pattern confirmed the formula of pure $Co_3[Fe(CN)_6]_2{\cdot}10H_2O$ (JCPDS 86–0502) (Fig. 1D) produced after preparation.

2.2 Imaging function of PBA

Iron-containing nanoparticles have been extensively studied as potential contrast agents for MRI.[43, 44] It has been reported that PB has extraordinary performance as an MRI contrast agent due to its special structure.[7, 28, 45] Nanostructures of PB contain low-spin Fe^{2+}-C (S= 0) and high-spin Fe^{3+}-N (S= 5/2), which could shorten the time of transverse and longitudinal relaxation on water protons. In addition, each Fe^{2+}-C ≡ N-Fe^{3+} unit of PB has five unpaired electrons that can form coordination bonds between water molecules and Fe^{3+}, causing relaxation inside PB and enhancing the contrast effect.[7] In this study, the synthesized PBA was considered to have a similar structure and character to PB, so this PBA was also expected to have the potential to be an MRI contrast agent. Figure 1E demonstrated that different concentrations of PBA displayed various degrees of T_2-weighted contrast property due to the Fe^{3+} superparamagnetic centers, and r^2 relaxation value was determined to be 61.381 $mM^{-1}s^{-1}$, implying that PBA is a prospective contrast agent for MRI.

PA is a new visual imaging technology based on light absorption-induced ultrasonic waves.[46–49] Because of the excellent performance on NIR region absorption, the PBA could also be used as a contrast agent for PA. The results are shown in Fig. 1F. As the PBA concentrations increased, the PA signal intensity was also enhanced and presented an almost linear increase. These results demonstrated that the PBA can be performed as a contrast agent for PA imaging.

2.3 Photothermal, photodynamic and chemodynamic effect of PBA

As shown in Fig. 2A, 1 mg mL^{-1} PBA presented a brownish black color and good dispersed in water. The UV-vis absorption spectrum showed that PBA had broad and strong absorption in NIR region (500–900 nm), which demonstrated that PBA had potential application as an NIR-driven photothermal agent. Subsequently, the photothermal effect of PBA was detected by temperature change of different concentrations of PBA under 808 nm irradiation for 10 min with PBS solution as a control. The temperature of PBA solution rapidly increased (7–40°C) with increasing time and concentrations (0.1-2 mg mL^{-1}), while control group had a negligible temperature change (3°C) (Fig. 2B). Moreover, the data showed that more than 0.5 mg mL^{-1} PBA can rapidly heat to hyperthermic conditions (> 45°C), which further demonstrated the photothermal ablation potential of PBA for cancer cells.[50] In addition, we also investigated the temperature changes of 1 mg mL^{-1} PBA with irradiation powers varying from 0.1 to 2 W cm^{-2}; the results showed a strong dependence on irradiation energy (Fig. 2C), and 2 W cm^{-2} irradiation was adopted in subsequent experiments. The photothermal stability of PBA was further studied by laser on/off experiments for five cycles. The results were presented in Fig. 2D, the temperature changes of PBA were similar in five cycles, which indicated the excellent photothermal stability of PBA. According to these data, the photothermal conversion efficiency of PBA was calculated, and the η value was approximately 41.44%, which demonstrated the excellent photothermal conversion performance of PBA.

The ·OH production was measured by MB and OPD probe. The diminish of MB indicates Fenton reaction occurred and diaminophenazine (DAP) can generate by OPD under Fenton reaction, both of these tests can detected at specific absorbance. As the results showed in Fig. 2E-F, the absorbance at 665 nm in MB solution were declined because of PBA treatment while at 452 nm absorbance, the OPD solution emerged a peak due to PBA caused Fenton reaction. Since the release of Fe^{2+} can cause Fenton reaction, the Fe^{2+} released of PBA was also evaluated. The result revealed that absorbance of 2,2'-bipyridine was decreased which confirmed Fe^{2+} releasing from PBA further lead to Fenton reaction (Fig. 2G). [51] GSH, as superoxide consumption in tumor environment which can relieve ROS induced cell death. Thus, the further experiment evaluated the PBA induced GSH depletion effect, result demonstrated PBA treatment can reduce GSH contents (Fig. 2H). To evaluate the $^1O_2$ generate capacity of PBA, the mixture with or without irradiation was measured by DPBF degradation test. The results displayed in Fig. 2I showed the content of DPBF was decreased rapidly to almost 50% under NIR irradiation compared to control group indicated the excellent PDT effect of PBA. The more declined of DPBF appeared in PBA + H_2O_2 + NIR group implied the synergy of PDT and CDT, which CDT process caused decomposition of H_2O_2 into O_2 and ·OH, and more O_2 lead to more PDT effect.

2.4 *In vitro* combined therapy effect of PBA

Because of the excellent performance of PBA for NIR response, the photoablation property *in vitro* was investigated in 4T1 cells by LIVE/DEAD™ staining. As shown in Fig. 3A, the living cells were dyed with

FITC, exhibiting green fluorescence, while the dead cells presented red fluorescence due to Texas Red staining. After PBA + NIR treatment, significant red fluorescence was observed under a fluorescence microscope, which demonstrated massive cell death. In contrast, PBA alone group exhibited green fluorescence caused by living cells, which was similar to PBS and PBS + NIR treatment groups.

Surprisingly, in addition to the photothermal property, the photodynamic and chemodynamic effect of the PBA was also observed in 4T1 cells through DCFH-DA staining. DCFH-DA is a commonly used dye to detect ROS based on oxidation reactions, and the generation of ROS will be marked by intense green fluorescence. Figure 3B displayed the images captured by fluorescence microscopy after different treatments. An evident comparison was observed in PBA + NIR and PBA + H_2O_2 + NIR groups with bright green fluorescence enhancement, while PBA + H_2O_2 exhibited slight fluorescence and the others showed almost no green fluorescence, which demonstrated that the PBA with laser irradiation and H_2O_2 could generate ROS effectively. The underlying mechanism may be based on laser-induced metal charger transfer from ground state to excited state. When the nanoparticle is in its excited state, the energy may stimulate the generation of $^1O_2$ from molecular oxygen so that the nanoparticle returns to the ground state. [52] Additionally, PBA released Fe^{2+} as a catalyst, participating in Fenton reaction with H_2O_2 as substrate and generating ·OH and O_2. ·OH is one of ROS could enhance fluorescence intensity and O_2 could give more substrate for PDT process.

Ferroptosis is one of cell death pathway which dependent on iron and ROS accumulation. Since Fe^{2+} released and ROS generated capacity of PBA was confirmed, it was considerable that the underlying mechanism was related with ferroptosis. Glutathione peroxidase (GPX4) as a critical enzyme in ferroptosis process, its activity can prevent the toxicity of lipid peroxide. The less content of GPX4 causes more serious ferroptosis of cell death. [53] Nuclear factor E2-related factor 2 (NRF2) is also an anti-ferroptosis factor. After PBA treatment, both of GPX4 and NRF2 were declined in 4T1 cells, indicated ferroptosis occurred (Fig. 3C-D). Additionally, iron metabolism pathway plays an important role in ferroptosis process. PBA could release lots of Fe^{2+} in tumor microenvironment which supplied more resource of Fe^{2+} for tumor cells and further disturbed iron metabolism. The results showed transferrin receptor 1 (TFR1), ferritin heavy chain 1 (FTH1) and ferritin light chain (FTL) were all increased after PBA treatment which demonstrated disorders of iron metabolism (Fig. 3E-G). Thus, PBA induced ferroptosis was caused by combined effect of down regulated GPX4, NRF2 and increased TFR1, FTH1, FTL, as well as Fenton reaction (Fig. 3H).

2.5 Combined treatment of PBA *in vivo*

To further confirm combined therapeutic effect of PBA *in vivo*, a tumor-bearing mouse model was established. Figure 4A presented the comparison of temperature change between PBS and PBA treatment with laser irradiation for 10 min. It was clear that PBA treatment could heat the tumor site above 45°C after 1 min of irradiation, while the control group remained at 37°C. More details were recorded in Fig. 4B. The temperature of PBA group dramatically rise to 55°C in 200 s irradiation and then increased slowly, and after treated for 400 s, the temperature of tumor site was maintained at approximately 60°C. In

contrast, the temperature of PBS group increased slowly during irradiation and finally remained at approximately 45°C.

According to the above results, the long-term combination therapeutic effect on PTT/PDT/CDT treatment of PBA was investigated *in vivo*. Tumor-bearing BALB/c mice were randomly divided into four groups: PBS, PBA, PBS + NIR and PBA + NIR. Figure 4C displayed the weight changes of mice in different groups, and no obvious difference was observed during whole process. Tumor volumes were recorded as V/V_0 in Fig. 4D. It was clearly demonstrated that after PBA injection and laser irradiation, the tumor was digested and cleaned up; more importantly, there was no tumor recurrence during the 27-day observation period. In contrast, the other three groups showed the same tumor growth rate, and final tumor size is intuitively presented in Fig. 4E. Compared to small recovered scab of PBA + NIR group tumor, the others were extremely huge. Figure 4F displayed pathological change of tumor after 24 h treated. The tumor treated with PBA + NIR exhibited a large amount of cell necrosis, while the tumors treated with PBS, PBA and PBS + NIR showed no obvious abnormalities. All the results supported the excellent combination therapy efficiency on PTT/PDT/CDT treatment of PBA for tumor.

2.6 Evaluation of PBA on tumor metastasis

The previous studies demonstrated that although some nanomaterials had a small impact on cancer cell proliferation, they impair the migration and metastasis of tumors.[40, 54–56] Hence, we also explored the effect of PBA on tumor metastasis *in vivo* and *in vitro*. After a 27-day observation experiment, the lungs of each mouse were harvested, and metastatic nodes were counted. The tumor metastatic nodes were clearly observed on the surface of lung (Fig. 5A), and a typical histopathological slice was presented by H&E staining (Fig. 5C). After PBS, PBA and PBS + NIR treatment, some dark dyed nodules with clear edges were observed in the lung tissue, which further confirmed the tumor metastasis. In addition, statistical data of metastatic node numbers in PBS- and PBA-treated groups were significantly different, which suggested the potential utility of this PBA as a synergistic anti-metastasis agent to suppress tumor invasion (Fig. 5B).

Further mechanistic exploration of PBA on tumor metastasis was also studied in 4T1 cells *in vitro*. The transwell experiment was used to confirm the effect of PBA on cell invasion. After treatment with 0, 10 and 50 μg mL^{-1} PBA for 24 h, the intensity of migrated cells was reduced after PBA treatment (Fig. 5D-E). These results combined with those in Fig. 4 showed that PBA had no significant effect on cytotoxicity without laser irradiation, which demonstrated that reduction of invasive cells in Fig. 5D was contributed by t tumor metastasis-preventing property of PBA.

EMT is a typical biological phenomenon in tumor metastasis and is also an important target for tumor therapeutic approaches. EMT is characterized by a decrease in cell adhesion and the expression of proteases such as matrix metalloproteinases (MMPs).[57] Epithelial cadherin, also called E-cadherin, is a tight junction molecule between cells, and the decomposition of E-cadherin induces tumor metastasis.[58] As shown in Fig. 5F-H, the expression of E-cadherin (CDH-1) was increased after PBA treatment, while that of MMP9 was decreased at the same time, which agreed with the results of the transwell experiment.

To summarize, PBA exhibited surprising potential for inhibition of tumor metastasis, which was confirmed by *in vitro* and *in vivo* experiments. The mechanism of decreased tumor invasion by PBA was achieved by suppressing MMP9 expression and recovering E-cadherin function.

2.7 Biodegradability and biocompatibility of PBA

Since more and more attention has been paid to application of nanomaterials for cancer diagnosis and treatment, safety concerns also appear at the same time. The most important issues are cytotoxicity, long-term bioaccumulation and nanoparticle aggregations caused vascular blockage.[24] Therefore, it is very meaningful to find materials with good biodegradability for use in body.[59, 60] Due to the biocompatibility and FDA approval of PB, this traditional dyestuff has been considered as a safe agent for PTT treatment of tumors. However, the long-term toxicity and physical aggregation of PB are still to be solved.[7] To evaluate the same problem in PBA, 1 mg mL^{-1} PBA was prepared in different solvents (distilled water, PBS, 10% FBS, 10% BSA and EDTA), among which 10% FBS and 10% BSA were used to simulate the internal environment. The results were recorded in Fig. 6A, and the images from day 0 to day 12 were displayed. The different tubes of prepared solutions on day 0 appeared to be uniform brownish black except for the pink color of EDTA tube (possibly due to chelation with Co^{2+} in PBA). After 3 days, the color of 10% FBS and 10% BSA groups gradually faded, especially on day 12; these two groups basically recovered to original solvent color, while the color of the others had no obvious change. These results suggested that the synthesized PBA may decompose gradually internally, but *in vivo* experiments are still needed to determine degradation effect and mechanism.

Besides that, the biocompatibility of PBA was evaluated by hemolysis test and results revealed that even 1 mg mL^{-1} PBA could remain the normal condition of erythrocyte compared positive control group (Figs. 6B). The biocompatibility of PBA was also investigated during cancer treatment, the major organs (heart, liver, spleen and kidney) were collected to weigh and stain with H&E. The final histograms and images are displayed in Fig. 6C-F and Fig. 7. Both the results showed that these organs had no noticeable pathological change during the 27-day observation, which demonstrated that no organ damage occurred after PBA treatment except in spleen. The abnormal performance of spleen could be induced by tumor development, which caused immune response in the whole body under PBS, PBA and PBS + NIR treatment.

3. Conclusions

In this study, a novel NIR photoreactive material, a PBA, was prepared via a facile protocol. The broad NIR absorption gave PBA potential for use in photothermal and photodynamic therapy for tumor treatment. Meanwhile, PBA also had ability for chemodynamic therapy due to Fenton reaction caused by ferrous ion and the underlying pathway was related to ferroptosis. Additionally, the PBA also exhibited excellent potential as MRI and PA contrast agents. More importantly, the outstanding biodegradation and anti-metastatic properties of PBA encouraged its use as a unique nanoparticle for cancer treatment. Further

exploration revealed that the underlying mechanism by which PBA suppressed cancer invasion was by regulating EMT protein expression.

4. Methods

4.1 Materials

Cobalt nitrate, potassium hexacyanoferrate(III) and sodium citrate were purchased from Sigma-Aldrich (USA). 4T1 cells were gained from American Type Culture Collection (USA). Dulbecco's Modified Eagle Media (DMEM), Fatal Bovine Serun (FBS), Phosphate Buffered Saline (PBS) and 4% paraformaldehyde were purchased from Gibco (USA). A ROS Assay Kit was purchased from Beyotime (China). A LIVE/DEAD^{TM} Cell Imaging Kit was obtained from Thermo Fisher Scientific (USA). A 24-well transwell plate was obtained from Corning (USA). Primary antibodies against MMP9, CDH-1 and GAPDH were obtained from ABclonal Technology (China). The secondary antibody was obtained from Abcam (USA).

4.2 Preparation of PBA

The synthesis of PBA was based on a precipitation method with slight modification.[41] The first step was the preparation of solution A and solution B: solution A was a mixture of 0.03 mol L^{-1} cobalt nitrate and 0.045 mol L^{-1} sodium citrate, while solution B was a 20 mL potassium hexacyanoferrate(III) (0.02 mol L^{-1}) solution. Then, solutions A and B were mixed by stirring for 1 min, and the obtained mixture was aged at room temperature for 18 h. Finally, the final PBA was obtained after centrifugation with water and ethanol.

4.3 Characterization of PBA

Scanning electron microscopy (SEM) (S-4800 FESEM, Hitachi, Japan) was used to investigate the surface of PBA. More information about the morphology and internal structure of PBA was provided by transmission electron microscopy (TEM) (JEM 2100F, JEOL, USA) and energy-dispersive X-ray spectroscopy (EDS) was presented by a Thermol UltraDry EDS system attached to the TEM instrument. The crystal structure of PBA was characterized by X-ray diffractometry (XRD) (X'Pert Pro MPD, PANalytical, Netherlands). The absorption spectrum was recorded by a UV-vis spectrophotometer (UV-1800, Shimadzu, China). MRI was obtained by a 3.0 T MR imaging instrument. Photoacoustic tomography (PAT) was collected on a multispectral optoacoustic tomography scanner (MSOT, iThera Medical, Germany).

4.4 Photothermalperformance

To investigate the photothermal properties of PBA, different concentrations of PBA (0.1 0.2, 0.5, 1, 2 mg mL^{-1}) were prepared and treated with 808 nm irradiation at various powers (0.1, 0.5, 1, 2 W cm^{-2}) for 6 min. The real-time temperature of sample was measured by an FLIR thermal camera. A laser on/off experiment was used to estimate the photothermal stability of PBA. The whole process included five

continuous cycles, each of which was under 808 nm irradiation at 2 W cm^{-2} for 600 s in the laser on condition, and then turned the laser off until the solution had cooled down to room temperature naturally. Furthermore, the photothermal conversion efficiency (η) of PBA was calculated.[12]

$$\eta = \frac{hS(T_{max} - T_{max,control})}{I(1-10^{-A_{808}})} \times 100\% \quad (1)$$

$$hS = \frac{m\ C}{\tau_S} \quad (2)$$

$$t = \tau_s \times \ln\theta \quad (3)$$

$$\theta = \frac{(T_{amb} - T)}{T_{amb} - T_{max}} \quad (4)$$

T_{max}: maximum equilibrium temperature for PBA solution

$T_{max,control}$: maximum equilibrium temperature for PBS

I: the incident laser power

A_{808}: absorbance of the PBA at 808 nm

m: mass of products

C: heat capacity of solvent

t: a series of constant cooling time corresponding of PBA solution

T: constant cooling temperature of PBA solution

T_{amb}: the ambient temperature of the surroundings

4.5 Extracellular·OH generation experiment

Three milligram PBA was added into 3 mL water, and then 20 μg mL^{-1} methylene blue (MB) and 100 μM H_2O_2 solutions were added. The ·OH generation was measured through the absorbance at 665 nm.

PBA was mixed with 10 mM *o*-phenylenediamine (OPD) and 100 μM H_2O_2 solution. The ·OH generation was measured through the absorbance at 452 nm.

4.6 Release of ferrous ions

The 2,2'-bipyridine was used to monitor ferrous ions release of PBA. The mixed solution which contained 6 mM 2,2'-bipyridine and 1 mg mL^{-1} PBA was prepared and the absorbance was detected at 520 nm after 12 h.

4.7 Depletion of glutathione (GSH)

5,5 -dithiobis-(2-nitrobenzoic acid, DTNB) was added to 1 mg mL^{-1} PBA solution which contained 0.01 M GSH. After 12 h, the absorbance was monitored at 412 nm.

4.8 *In vitro* photodynamic property

1,3-diphenylisobenzofuran (DPBF) was added to PBA solution under irradiation for 0, 5, 10, 20 min and the release of $^1O_2$ was detected through DPBF contents at 420 nm absorbance.

4.9 *In vitro* photothermal property

First, 4T1 cells were seeded into 96-well plates overnight and divided into four groups: PBS, PBS+NIR, PBA and PBA+NIR groups. Then, the culture media were removed by rinsing with PBS three times, and the samples were treated as follows: the PBA and PBA+NIR groups were treated with culture medium which contained 1 mg mL^{-1} PBA, and the PBS and NIR groups were treated with the same dosage of culture medium contained PBS. After incubated for 4 h, the media were removed, and the samples were rinsed with PBS three times, and then the PBS+NIR and PBA+NIR groups were accepted 808 nm irradiation at 2 W cm^{-2} for 10 min. Last, all of these groups were dyed with the LIVE/DEAD^{TM} Cell Imaging Kit which the green fluorescence exhibited living cells, while dead cells were marked red.

4.10 Intracellular reactive oxygen species (ROS) generation

The pretreatment process with 4T1 cells was similar to the LIVE/DEAD^{TM} Cell Imaging Kit experiment. Then, the ROS Assay Kit was used to detect intracellular ROS generation. The DCFH-DA probe was diluted in FBS-free DMEM (10 μmol L^{-1}) and replaced with culture medium. After culturing for another 20 min, all groups were washed with FBS-free DMEM three times, and then NIR groups were treated with 808 nm irradiation at 2 W cm^{-2} for 10 min. All groups were recorded by fluorescence microscopy.

4.11 Quantitative polymerase chain reaction (qPCR) experiment

After treated with different concentrations of PBA and 100 μM H_2O_2, the total RNA of 4T1 cells were extracted. Then, cDNA were reversed using *Evo M-MLV* RT Premix Kit (Accurate Biotechnology Co., Ltd) and SYBR Green Premix *Pro Taq* HS qPCR Kit (Accurate Biotechnology Co., Ltd) was used for qPCR. The

specific primers in this study were deigned as: mouse GAPDH forward primer: 5'-ACCCTTAAGAGGGATGCTGC-3'; mouse GAPDH reverse primer: 5'-CCCAATACGGCCAAATCCGT-3'; mouse GPx4 forward primer: 5'-GCCTGGATAAGTACAGGGGT-3'; mouse GPx4 reverse primer: 5'-ACCACACTCAGCATATCGGG-3'; mouse Nrf2 forward primer: 5'-AGATGACCATGAGTCGCTTGC-3'; mouse Nrf2 reverse primer: 5'-GCCAAACTTGCTCCATGTCC-3'; mouse TfR1 forward primer: 5'-GTGATTGTTAGAGCAGGGGA-3'; mouse TfR1 reverse primer: CTGATGACTGAGATGGCGGA-3';mouse FTH1 forward primer: 5'-GCCGAGAAACTGATGAAGCTGC-3'; mouse FTH1 reverse primer: 5'-GCACACTCCATTGCATTCAGCC-3'; mouse FTL forward primer: 5'-CACCTACCTCTCTCTGGGCT-3'; mouse FTL reverse primer: 5'-CGCGATCGTTCTGAAACTCG-3'. Parameter setting as: pre incubation at 95 ^{o}C for 30 s then amplification at 95 ^{o}C for 1 min, 30 ^{o}C for 55 s and 97 ^{o}C for 1s, cooling at 37 ^{o}C for 30 s. The process was continued for 40 cycles. The Ct values were corrected through GAPDH Ct value.

4.12 Tumor-bearing mouse model

BALB/c mice (4-5 weeks, female) were obtained from Guangdong Medical Laboratory Animal Center, and all animal studies followed the guidelines approved by the ethics committee of Guangdong Medical Laboratory Animal Center (B202009-1). All applicable institutional or national guidelines for the care and use of animals were followed. After adaptive feeding for one week, all mice were injected with 100 μL 3×10^{6} 4T1 cell suspension. All tumor interferences were carried out when the tumor size reached about $5*5^{2}$ (length*width^{2}) mm^{3}.

4.13 Evaluation of the photothermal effect *in vivo*

When the tumor-bearing mouse models were successfully established, they were divided into PBS+NIR and PBA+NIR groups randomly, and 50 μL PBS or PBA (10 mg mL^{-1}) was injected into the tumor site. After that, the mice were exposed under 808 nm irradiation at 1 W cm^{-2} for 10 min. The real-time temperature change and images of the whole mouse body were recorded on an FLIR thermal camera.

4.14 Animal experiment

The tumor-bearing BALB/c mice were divided into four groups: PBS, PBS+NIR, PBA and PBA+NIR groups. The PBS and PBS+NIR groups were injected with 50 μL PBS into the tumor site, while the PBA and PBA+NIR groups were injected with 10 mg mL^{-1} PBA into the tumor site at the same dosage. Both the PBS+NIR and PBA+NIR groups underwent irradiation treatment at 808 nm for 10 min. The tumor samples of each group were harvested with H&E staining after treatment for 24 h to estimate the pathological changes. Other tumor-bearing mice were monitored, and the tumor sizes were determined to calculate the tumor volumes (tumor volumes=length×width^{2}/2). Twenty-seven days after treatment, several major organs were collected for H&E staining treated, and tumor metastasis numbers in the lung were counted and analyzed.

4.15 Antitumor metastasis potential *in vitro*

Transwell experiments were used to evaluate the antitumor metastasis effect of PBA. First, FBS-free DMEM was replaced with culture medium for 24 h. Then, 1×10^5/well 4T1 cells were incubated on the upper compartment of 24-well transwell plates with different concentrations of PBA (0, 10, 50 μg mL^{-1}), and the lower chambers were filled with 20% FBS-culture medium at the same time. After incubation for 24 h, the cells that remained in the upper compartment were wiped with a cotton swab, while the cells that migrated through the membrane were fixed with 4% paraformaldehyde for 30 min, stained with 0.1% crystal violet and observed under a light microscope.

To further prove the antitumor metastasis effect, a western blot experiment was performed. After 4T1 cells were incubated with PBA (0, 10, 50 μg mL^{-1}) for 24 h, the cells were rinsed with cold PBS twice and collected. Then, 8% SDS-PAGE electrophoresis was used to separate and identify total protein. After that, the targeted bands were transferred to PVDF membranes and blocked. Primary antibodies against MMP9, CDH-1 and GAPDH were added to distinguish the targeted protein at 4 °C overnight, and secondary antibodies were cultured for another 2 h at room temperature. Finally, the targeted protein was visualized with an ECL Western Blotting Detection Kit.

4.16 Hemolysis test

The fresh blood was collected and centrifuged under 2000 rpm for 5 min. Then, the 2% erythrocyte suspension was prepared. Several PBA solutions were added to 2% erythrocyte suspension at 37 °C for 1 h and recorded after 2000 rpm centrifugation.

4.17 Biodegradability of PBA

Several solvent systems were prepared to investigate the biodegradability of PBA, including distilled water, PBS, 10% FBS, 10% Bovine Serum Albumin (BSA) and Ethylene Diamine Tetraacetic Acid (EDTA). Then, 1 mg mL^{-1} PBA was prepared in the different solvents and placed at room temperature.

4.18 Statistical analysis

All the data in this report were collected and analyzed by IBM SPSS Statistics 20.0, and the quantitative data were organized as the mean ± standard deviation (SD). One-way ANOVA was used to investigate the comparison among groups. $P<0.05$ was considered a significant difference.

Declarations

Ethics approval and consent to participate

All animal studies followed the guidelines approved by the ethics committee of Guangdong Medical Laboratory Animal Center (B202009-1).

Consent for publication

All authors are consent for publication.

Availability of data and materials

The datasets used and/or analyzed during the current study are available from the corresponding author on reasonable request.

Competing interests

The authors in this work declare no conflict interests.

Funding

This work was supported by National Natural Science Foundation of China [grant number: 81973013, 81972488, 81701836], Guangdong Key R&D Program [grant number: 2019B020210002], Natural Science Foundation of Guangdong Province [grant number: 2018030310301] and the Eighth Affiliated Hospital of Sun Yat-sen University Outstanding Youth Reserve Talent Science Fund [grant number: FBJQ2019002].

Authors' contributions

Miaomiao Yuan and Wenzhen Liao designed this project. Yuting Hao, Lianzhi Mao and Rongjun Zhang performed the experiment and Yuting Hao wrote the paper. Xiaoshan Liao analyzed the data. All authors commented on the paper.

Acknowledgements

Not applicable.

References

1. Hartshorn CM, Bradbury MS, Lanza GM, Nel AE, Rao J, Wang AZ, Wiesner UB, Yang L, Grodzinski P: **Nanotechnology Strategies To Advance Outcomes in Clinical Cancer Care.***ACS Nano* 2018, **12:**24-43.
2. Catala L, Mallah T: **Nanoparticles of Prussian blue analogs and related coordination polymers: from information storage to biomedical applications.***Coord Chem Rev* 2017, **346:**32-61.
3. Dawidczyk CM, Kim C, Park JH, Russell LM, Lee KH, Pomper MG, Searson PC: **State-of-the-art in design rules for drug delivery platforms: lessons learned from FDA-approved nanomedicines.***J Control Release* 2014, **187:**133-144.
4. Xue P, Yang R, Sun L, Li Q, Zhang L, Xu Z, Kang Y: **Indocyanine Green-Conjugated Magnetic Prussian Blue Nanoparticles for Synchronous Photothermal/Photodynamic Tumor Therapy.***Nanomicro Lett* 2018, **10:**74.
5. Zou L, Wang H, He B, Zeng L, Tan T, Cao H, He X, Zhang Z, Guo S, Li Y: **Current Approaches of Photothermal Therapy in Treating Cancer Metastasis with Nanotherapeutics.***Theranostics* 2016, **6:**762-772.

6. Ke H, Wang J, Dai Z, Jin Y, Qu E, Xing Z, Guo C, Yue X, Liu J: **Gold-nanoshelled microcapsules: a theranostic agent for ultrasound contrast imaging and photothermal therapy.***Angew Chem Int Ed Engl* 2011, **50:**3017-3021.
7. Gautam M, Poudel K, Yong CS, Kim JO: **Prussian blue nanoparticles: Synthesis, surface modification, and application in cancer treatment.***Int J Pharm* 2018, **549:**31-49.
8. Long J, Guari Y, Guerin C, Larionova J: **Prussian blue type nanoparticles for biomedical applications.***Dalton Trans* 2016, **45:**17581-17587.
9. Cheng L, Yang K, Chen Q, Liu Z: **Organic stealth nanoparticles for highly effective in vivo near-infrared photothermal therapy of cancer.***Acs Nano* 2012, **6:**5605-5613.
10. Tian Q, Jiang F, Zou R, Liu Q, Chen Z, Zhu M, Yang S, Wang J, Wang J, Hu J: **Hydrophilic Cu9S5 nanocrystals: a photothermal agent with a 25.7% heat conversion efficiency for photothermal ablation of cancer cells in vivo.***ACS Nano* 2011, **5:**9761-9771.
11. Luo D, Carter KA, Miranda D, Lovell JF: **Chemophototherapy: An Emerging Treatment Option for Solid Tumors.***Adv Sci (Weinh)* 2017, **4:**1600106.
12. Hou M, Yan C, Chen Z, Zhao Q, Yuan M, Xu Y, Zhao B: **Multifunctional NIR-responsive PVP-Cu-Sb-S nanotheranostic agent for photoacoustic imaging and photothermal/photodynamic therapy.***Acta Biomater* 2018, **74:**334-343.
13. Liu Y, Zhen W, Jin L, Zhang S, Sun G: **All-in-One Theranostic Nanoagent with Enhanced Reactive Oxygen Species Generation and Modulating Tumor Microenvironment Ability for Effective Tumor Eradication.** 2018, **12:**4886-4893.
14. Liu C, Wang D, Zhang S, Cheng Y, Yang F, Xing Y, Xu T: **Biodegradable Biomimic Copper/Manganese Silicate Nanospheres for Chemodynamic/Photodynamic Synergistic Therapy with Simultaneous Glutathione Depletion and Hypoxia Relief.** 2019, **13:**4267-4277.
15. Kim J, Cho HR, Jeon H, Kim D, Song C, Lee N, Choi SH, Hyeon T: **Continuous O2-Evolving MnFe2O4 Nanoparticle-Anchored Mesoporous Silica Nanoparticles for Efficient Photodynamic Therapy in Hypoxic Cancer.***J Am Chem Soc* 2017, **139:**10992-10995.
16. Fingar VH: **Vascular effects of photodynamic therapy.***J Clin Laser Med Surg* 1996, **14:**323-328.
17. Tang Z, Liu Y, He M, Bu W: **Chemodynamic Therapy: Tumour Microenvironment-Mediated Fenton and Fenton-like Reactions.** 2019, **58:**946-956.
18. Ranji-Burachaloo H, Gurr PA, Dunstan DE, Qiao GG: **Cancer Treatment through Nanoparticle-Facilitated Fenton Reaction.***ACS Nano* 2018, **12:**11819-11837.
19. Yang P, Zhang S, Zhang N, Wang Y, Zhong J, Sun X, Qi Y, Chen X, Li Z, Li Y: **Tailoring Synthetic Melanin Nanoparticles for Enhanced Photothermal Therapy.***ACS Appl Mater Interfaces* 2019, **11:**42671-42679.
20. Xie L, Wang G, Zhou H, Zhang F, Guo Z, Liu C, Zhang X, Zhu L: **Functional long circulating single walled carbon nanotubes for fluorescent/photoacoustic imaging-guided enhanced phototherapy.***Biomaterials* 2016, **103:**219-228.

21. TaoGuo, YanLin, ZhiLi, ShanChen, GuomingHuang, HuirongLin, JunWang, GangLiu, Huang-HaoYang: **Gadolinium oxysulfide-coated gold nanorods with improved stability and dual-modal magnetic resonance/photoacoustic imaging contrast enhancement for cancer theranostics.***Nanoscale* 2017, **9:**56-61.
22. Bharathiraja S, Bui NQ, Manivasagan P, Moorthy MS, Mondal S, Seo H, Phuoc NT, Vy Phan TT, Kim H, Lee KD, Oh J: **Multimodal tumor-homing chitosan oligosaccharide-coated biocompatible palladium nanoparticles for photo-based imaging and therapy.***Sci Rep* 2018, **8:**500.
23. Liang X, Deng Z, Jing L, Li X, Dai Z, Li C, Huang M: **Prussian blue nanoparticles operate as a contrast agent for enhanced photoacoustic imaging.***Chemical Communications* 2013, **49:**11029.
24. Paris JL, Baeza A, Vallet-Regi M: **Overcoming the stability, toxicity, and biodegradation challenges of tumor stimuli-responsive inorganic nanoparticles for delivery of cancer therapeutics.***Expert Opin Drug Deliv* 2019, **16:**1095-1112.
25. Patra, Ranjan C: **Prussian blue nanoparticles and their analogues for application to cancer theranostics.***Nanomedicine* 2016, **11:**569-572.
26. Shokouhimehr M, Soehnlen ES, Hao J, Griswold M, Flask C, Fan X, Basilion JP, Basu S, Huang SD: **Dual purpose Prussian blue nanoparticles for cellular imaging and drug delivery: a new generation of T1-weighted MRI contrast and small molecule delivery agents.***Journal of Materials Chemistry* 2010, **20:**5251-5259
27. Fu G, Liu W, Li Y, Jin Y, Jiang L, Liang X, Feng S, Dai Z: **Magnetic Prussian blue nanoparticles for targeted photothermal therapy under magnetic resonance imaging guidance.***Bioconjug Chem* 2014, **25:**1655-1663.
28. Giacomo D, Angelo T, Piersandro P: **Prussian Blue Nanoparticles as a Versatile Photothermal Tool.***Molecules* 2018, **23:**1414.
29. Jiang Y, Takahashi A, Kawamoto T, Asai M, Zhang N, Lei Z, Zhang Z, Kojima K, Imoto K, Nakagawa K: **High performance sorption and desorption behaviours at high working temperatures of ammonia gas in a cobalt-substituted Prussian blue analogue.***Chemical Communications* 2018, **54:**11961-11964.
30. Xue P, Cheong KK, Wu Y, Kang Y: **An in-vitro study of enzyme-responsive Prussian blue nanoparticles for combined tumor chemotherapy and photothermal therapy.***Colloids Surf B Biointerfaces* 2015, **125:**277-283.
31. ; NS, Ohkoshi; S-i, Sato; O, Hashimoto K: **Control of Charge-Transfer-Induced Spin Transition Temperature onCobalt–Iron Prussian Blue Analogues.***Inorganic Chemistry* 2002, **41:**678-684.
32. Veiseh O, Kievit FM, Ellenbogen RG, Zhang M: **Cancer cell invasion: treatment and monitoring opportunities in nanomedicine.***Adv Drug Deliv Rev* 2011, **63:**582-596.
33. LYNCH HT, FUSARO RM, LYNCH JF: **Cancer: Genetics and the Environment. .***Ann N Y Acad Sci* 1997, **833:**1-209.
34. Liang C, Xu L, Song G, Liu Z: **Emerging nanomedicine approaches fighting tumor metastasis: animal models, metastasis-targeted drug delivery, phototherapy, and immunotherapy.***Chem Soc Rev* 2016,

45:6250-6269.

35. Schroeder A, Heller DA, Winslow MM, Dahlman JE, Pratt GW, Langer R, Jacks T, Anderson DG: **Treating metastatic cancer with nanotechnology.***Nat Rev Cancer* 2011, **12:**39-50.
36. Chen B, Wang C, Haijun Z: **Gambogic acid-loaded magnetic Fe3O4 nanoparticles inhibit Panc-1 pancreatic cancer cell proliferation and migration by inactivating transcription factor ETS1.***Int J Nanomedicine* 2012, **7:**781-787.
37. Chi X, Yin Z, Jin J, Li H, Zhou J, Zhao Z, Zhang S, Zhao W, Xie C, Li J, et al: **Arsenite-loaded nanoparticles inhibit the invasion and metastasis of a hepatocellular carcinoma: in vitro and in vivo study.***Nanotechnology* 2017, **28:**445101.
38. Wang C, Xu L, Liang C, Xiang J, Peng R, Liu Z: **Immunological responses triggered by photothermal therapy with carbon nanotubes in combination with anti-CTLA-4 therapy to inhibit cancer metastasis.***Adv Mater* 2014, **26:**8154-8162.
39. Liang C, Diao S, Wang C, Gong H, Liu T, Hong G, Shi X, Dai H, Liu Z: **Tumor metastasis inhibition by imaging-guided photothermal therapy with single-walled carbon nanotubes.***Adv Mater* 2014, **26:**5646-5652.
40. Tran TA, Krishnamoorthy K, Cho SK, Kim SJ: **Inhibitory Effect of Zinc Sulfide Nanoparticles Towards Breast Cancer Stem Cell Migration and Invasion.***J Biomed Nanotechnol* 2016, **12:**329-336.
41. Han L, Yu XY, Lou XW: **Formation of Prussian-Blue-Analog Nanocages via a Direct Etching Method and their Conversion into Ni-Co-Mixed Oxide for Enhanced Oxygen Evolution.***Adv Mater* 2016, **28:**4601-4605.
42. Cafun JD, Champion G, Arrio M-A, dit Moulin CC, Bleuzen A: **Photomagnetic CoFe Prussian Blue Analogues: Role of the Cyanide Ions as Active Electron Transfer Bridges Modulated by Cyanide? Alkali Metal Ion Interactions.***J Am Chem Soc* 2010, **132:**11552-11559.
43. Li Y, Xie Y, Wang Z, Zang N, Carniato F, Huang Y, Andolina CM, Parent LR, Ditri TB, Walter ED, et al: **Structure and Function of Iron-Loaded Synthetic Melanin.***ACS Nano* 2016, **10:**10186-10194.
44. Li Y, Huang Y, Wang Z, Carniato F, Xie Y, Patterson JP, Thompson MP, Andolina CM, Ditri TB, Millstone JE, et al: **Polycatechol Nanoparticle MRI Contrast Agents.***Small* 2016, **12:**668-677.
45. Li Z, Zeng Y, Zhang D, Wu M, Wu L, Huang A, Yang H, Liu X, Liu J: **Glypican-3 antibody functionalized Prussian blue nanoparticles for targeted MR imaging and photothermal therapy of hepatocellular carcinoma.***Journal of Materials Chemistry B* 2014, **2:**3686.
46. Wang LV, Hu S: **Photoacoustic tomography: in vivo imaging from organelles to organs.***Science* 2012, **335:**1458-1462.
47. Wang LV: **Prospects of photoacoustic tomography.***Med Phys* 2008, **35:**5758-5767.
48. Geng K, Zhou M, Song S, Huang Q, Li C: **Copper Sulfide Nanoparticles As a New Class of Photoacoustic Contrast Agent for Deep Tissue Imaging at 1064 nm.***Acs Nano* 2012, **6:**7489-7496.
49. Luke GP, Yeager D, Emelianov SY: **Biomedical applications of photoacoustic imaging with exogenous contrast agents.***Ann Biomed Eng* 2012, **40:**422-437.

50. Qing-Lan L, Yao S, Li R, Xin W, Chen W, Lin L, Ying-Wei Y, Xianghui Y, Jihong Y: **Supramolecular Nanosystem Based on Pillararene-Capped CuS Nanoparticles for Targeted Chemo-Photothermal Therapy.***ACS Applied Materials & Interfaces* 2018, **10:**29314-29324.
51. Zhang Q, Guo Q, Chen Q, Zhao X, Pennycook SJ, Chen H: **Highly Efficient 2D NIR-II Photothermal Agent with Fenton Catalytic Activity for Cancer Synergistic Photothermal-Chemodynamic Therapy.** 2020, **7:**1902576.
52. Wojde? JC: **First principles calculations on the influence of water-filled cavities on the electronic structure of Prussian Blue.** 2009, **15:**567-572.
53. Xie Y, Hou W, Song X, Yu Y, Huang J, Sun X, Kang R, Tang D: **Ferroptosis: process and function.***Cell Death Differ* 2016, **23:**369-379.
54. Karuppaiya P, Satheeshkumar E, Chao WT, Kao LY, Chen EC, Tsay HS: **Anti-metastatic activity of biologically synthesized gold nanoparticles on human fibrosarcoma cell line HT-1080.***Colloids Surf B Biointerfaces* 2013, **110:**163-170.
55. Wang Y, Yang F, Zhang HX, Zi XY, Pan XH, Chen F, Luo WD, Li JX, Zhu HY, Hu YP: **Cuprous oxide nanoparticles inhibit the growth and metastasis of melanoma by targeting mitochondria.***Cell Death Dis* 2013, **4:**e783.
56. Zheng W, Yang L, Liu Y, Qin X, Zhou Y, Zhou Y, Liu J: **Mo polyoxometalate nanoparticles inhibit tumor growth and vascular endothelial growth factor induced angiogenesis.***Sci Technol Adv Mater* 2014, **15:**035010.
57. Sistigu A, Di Modugno F, Manic G, Nistico P: **Deciphering the loop of epithelial-mesenchymal transition, inflammatory cytokines and cancer immunoediting.***Cytokine Growth Factor Rev* 2017, **36:**67-77.
58. Das B, Sarkar N, Bishayee A, Sinha D: **Dietary phytochemicals in the regulation of epithelial to mesenchymal transition and associated enzymes: A promising anticancer therapeutic approach.***Semin Cancer Biol* 2019, **56:**196-218.
59. Liu X, Wei D, Zhong J, Ma M, Zhou J, Peng X, Ye Y, Sun G, He D: **Electrospun Nanofibrous P(DLLA-CL) Balloons as Calcium Phosphate Cement Filled Containers for Bone Repair: in Vitro and in Vivo Studies.***ACS Appl Mater Interfaces* 2015, **7:**18540-18552.
60. Xu N, Ye X, Wei D, Zhong J, Chen Y, Xu G, He D: **3D artificial bones for bone repair prepared by computed tomography-guided fused deposition modeling for bone repair.***ACS Appl Mater Interfaces* 2014, **6:**14952-14963.

Figures

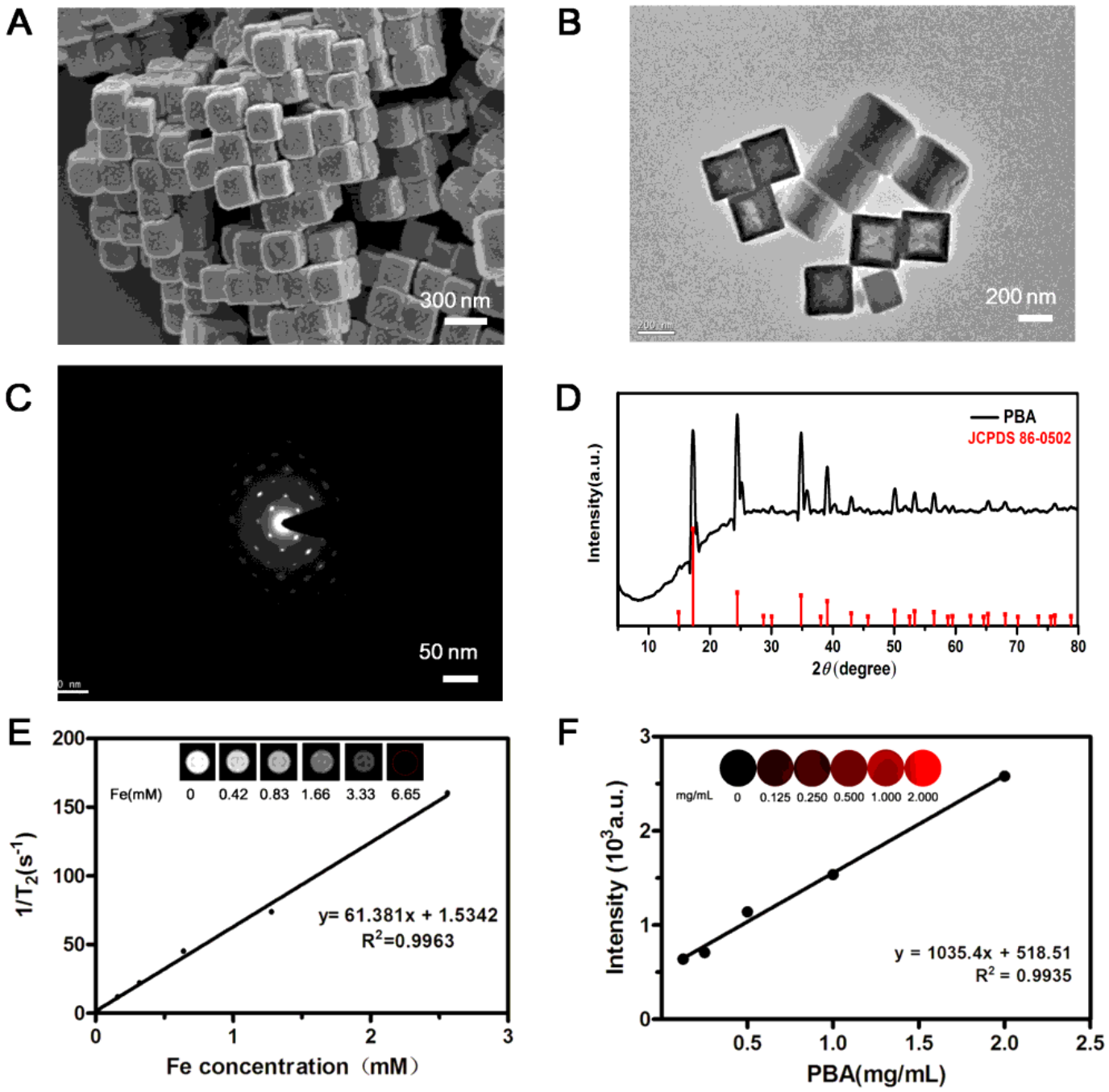

Figure 1

The characterization of prepared PBA. SEM (A) and TEM (B) image of PBA. Clear lattice structure of PBA recorded by TEM with EDS system (C). The XRD curve of PBA in comparison with the standard peak of Co3[Fe (CN)6]2•10H2O (JCPDS 86-0502) (D). Linear relationship between different concentratons of PBA and longitudinal relaxation time (E) and PA signal intensity (F).

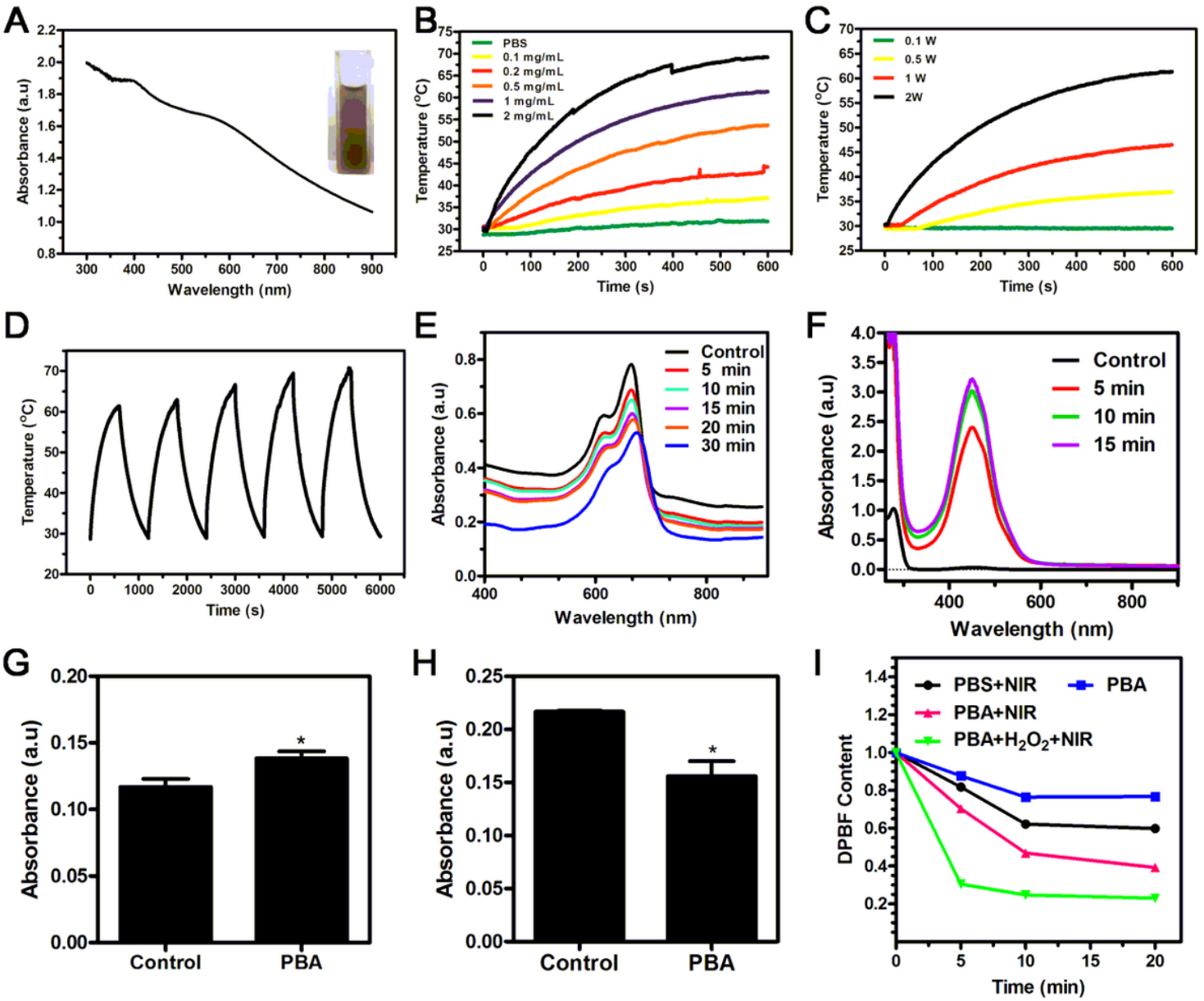

Figure 2

The physical properties of PBA. The broad and strong NIR absorption spectrum of PBA with the image of 1mg mL-1 PBA solution presented on the top right (A). The photothermal effect of PBA with different concentrations (B) and different powers of laser (C), both of them showed the temperature rise of PBA was dose dependent and laser power dependent. Photothermal stability of PBA was demonstrated through laser on/off experiment for five cycles, each of which was under 600s laser on condition then turned the laser off until the solution cooled to the room temperature (D). The absorbance changes of MB (E) or OPD (F) solution with PBA for different time. Ferrous ion released from PBA detected through 2,2'-bipyridine (G). The decrease of DTNB solution absorbance revealed GSH depletion property of PBA (H). The consumption of DTNB content revealed 1O2 generate capacity of PBA (I).

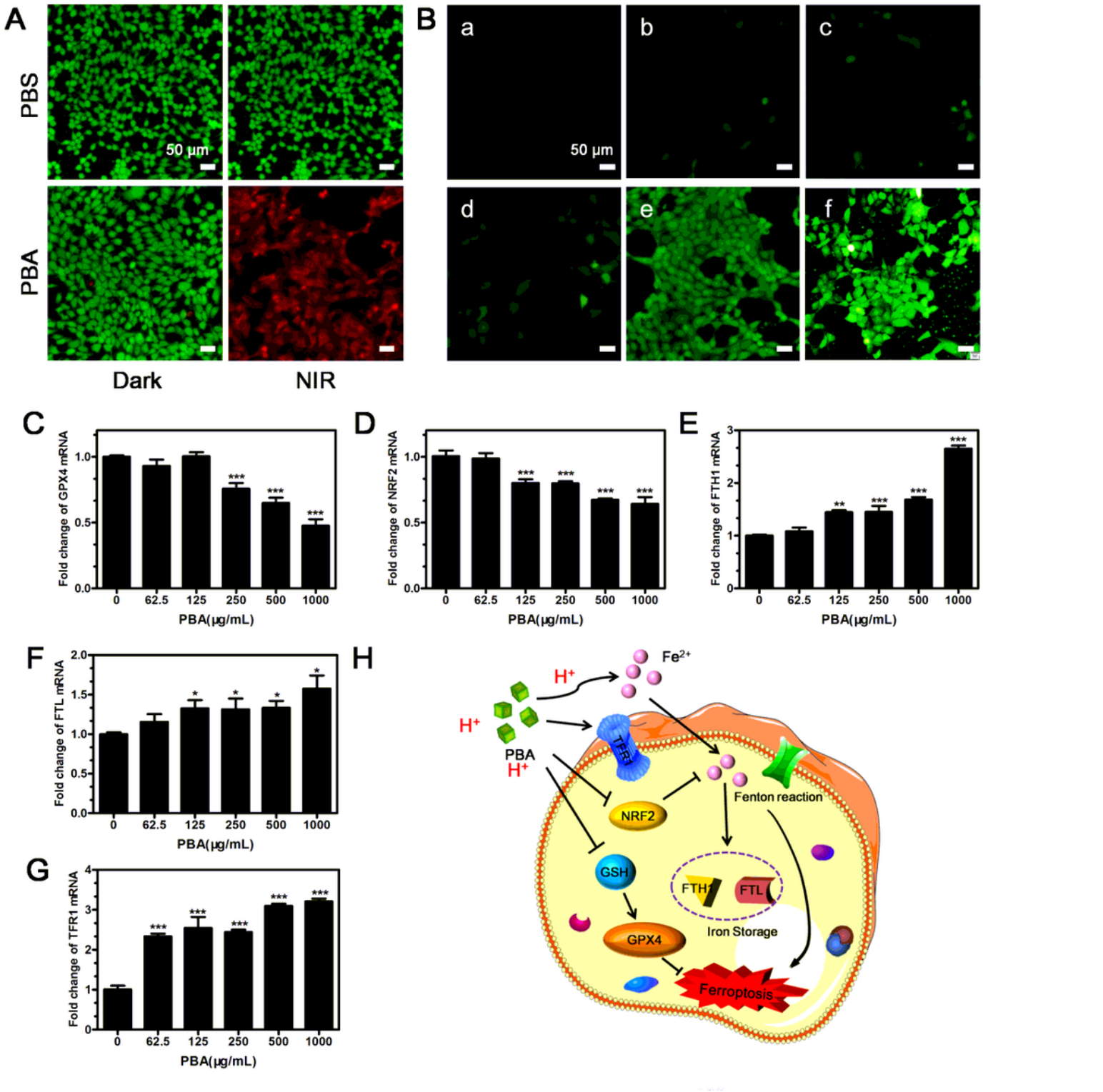

Figure 3

In vitro combined therapy effect of PBA. LIVE/DEADTM staining of 4T1 cells treated with PBS, PBS+NIR, PBA or PBA+NIR, which living cells were dyed with FITC (green) and dead cells were marked with Texas Red (red) (A). ROS generation of 4T1 cells after PBS (a), H2O2 (b), PBA (c), PBA+ H2O2 (d), PBA+NIR (e) or PBA+ H2O2+NIR (f) treatment, which ROS were monitored by DCFH-DA (green) (B). The fold change of

GPX4 (C), NRF2 (D), FTH1 (E), FTL (F) and TFR1 (G) mRNA of PBA-treated 4T1 cells. Possible ferroptosis pathway caused by PBA treatment (H).

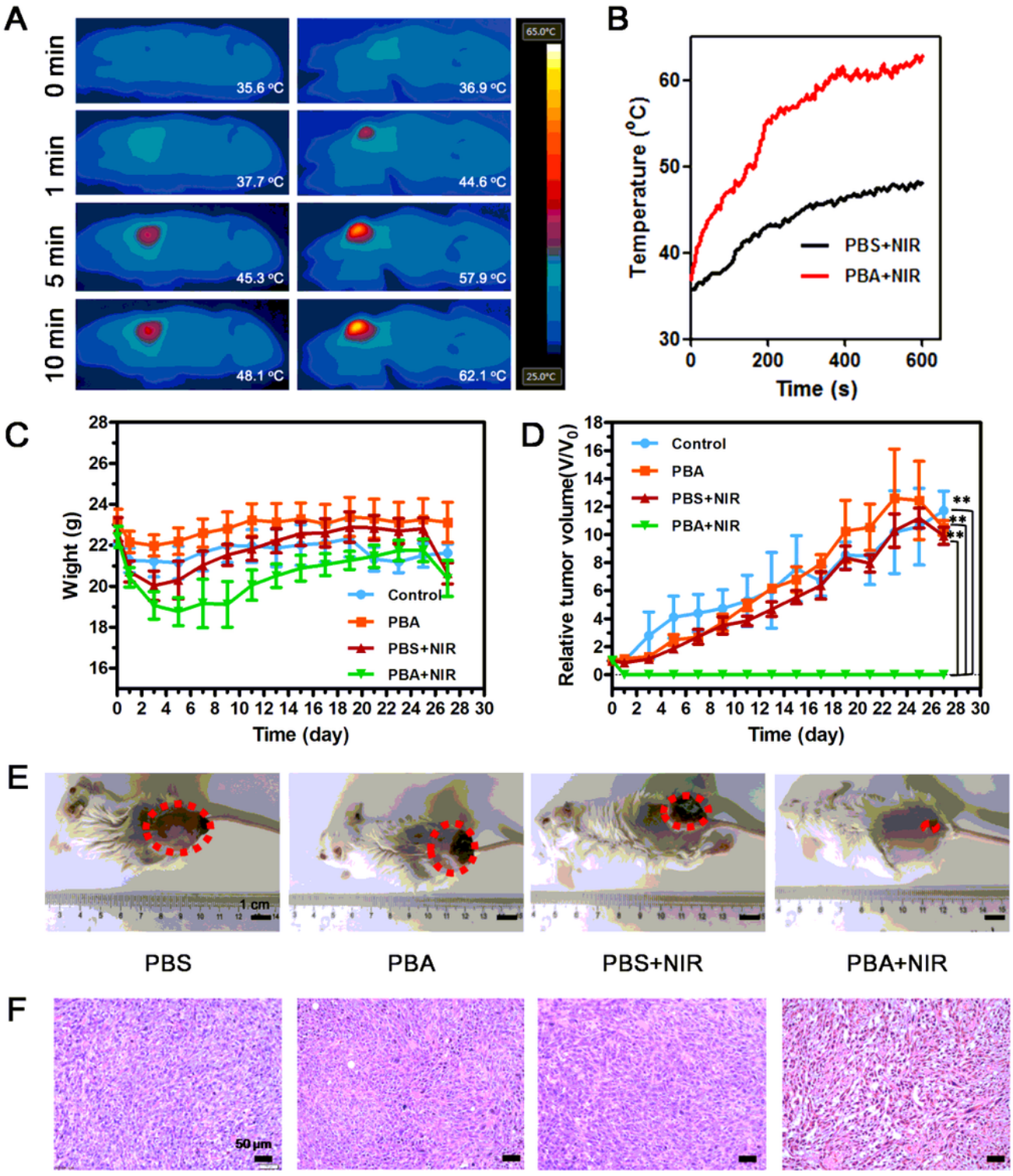

Figure 4

Photothermal therapy effect of PBA in vivo. The comparison of temperature change between PBS+NIR (left) and PBA+NIR (right) treatment (A) and the time-temperature curve was recorded in part (B). The weight change (C) and tumor volume increase curve (D) in whole observation period were demonstrated,

respectively. After 27-day observation, the intuitive images and corresponding pathological sections of tumors were presented (E-F). **P<0.01

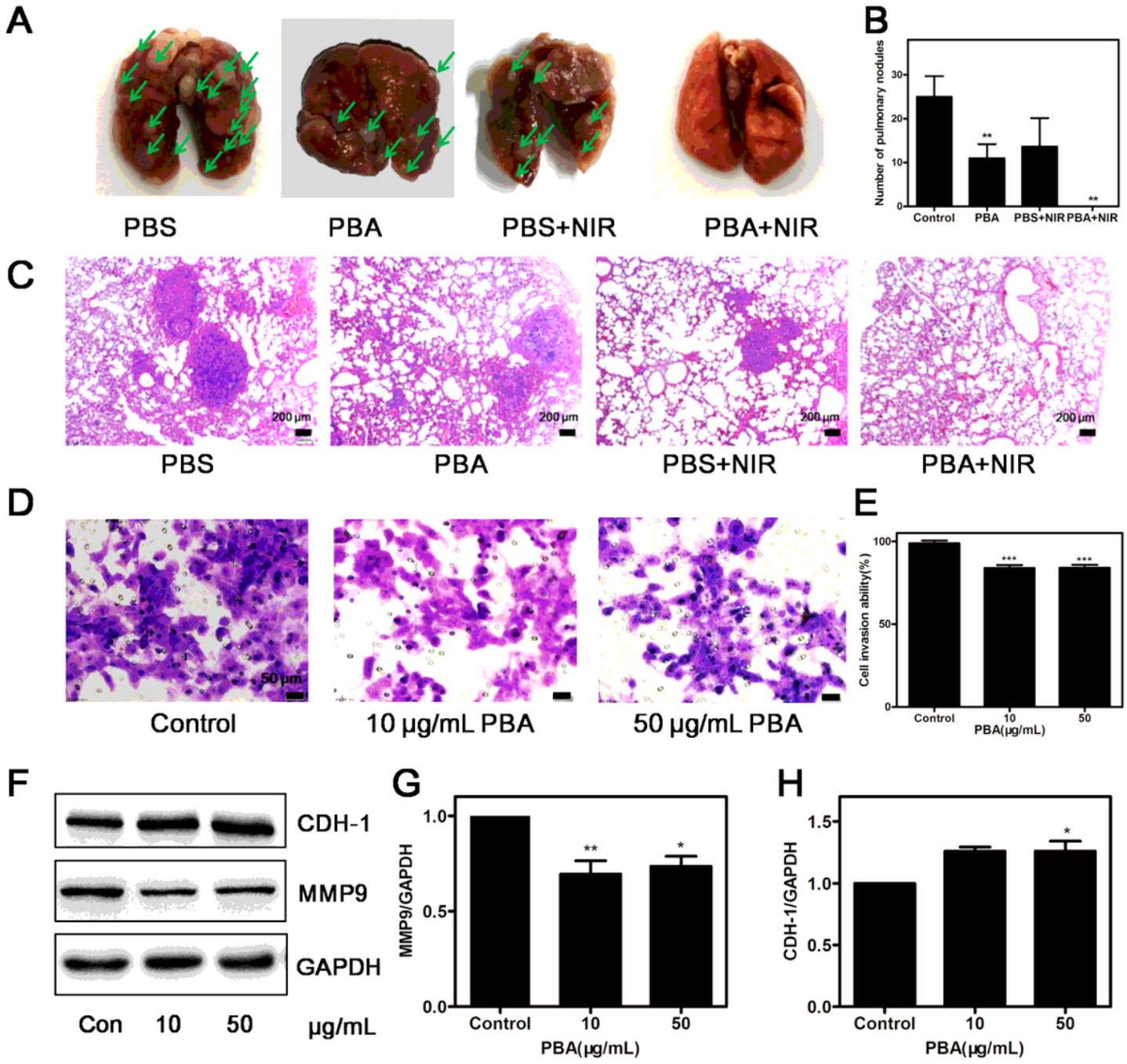

Figure 5

Anti-metastasis effect of PBA. After 27-day observation, the metastatic nodes on the surface of lung were recorded (A) (where the green arrows indicates the tumor nodes) and counted (B). Corresponding pathological section of lung clearly demonstrated the tumor nodules (C). Transwell (D) and Western Blot experiment (F) was used to explore further mechanism for anti-metastasis effect of PBA. And the transwell and WB statistical results are also showed in part (E, G-H). **P<0.05, **P<0.01, ***P<0.001.

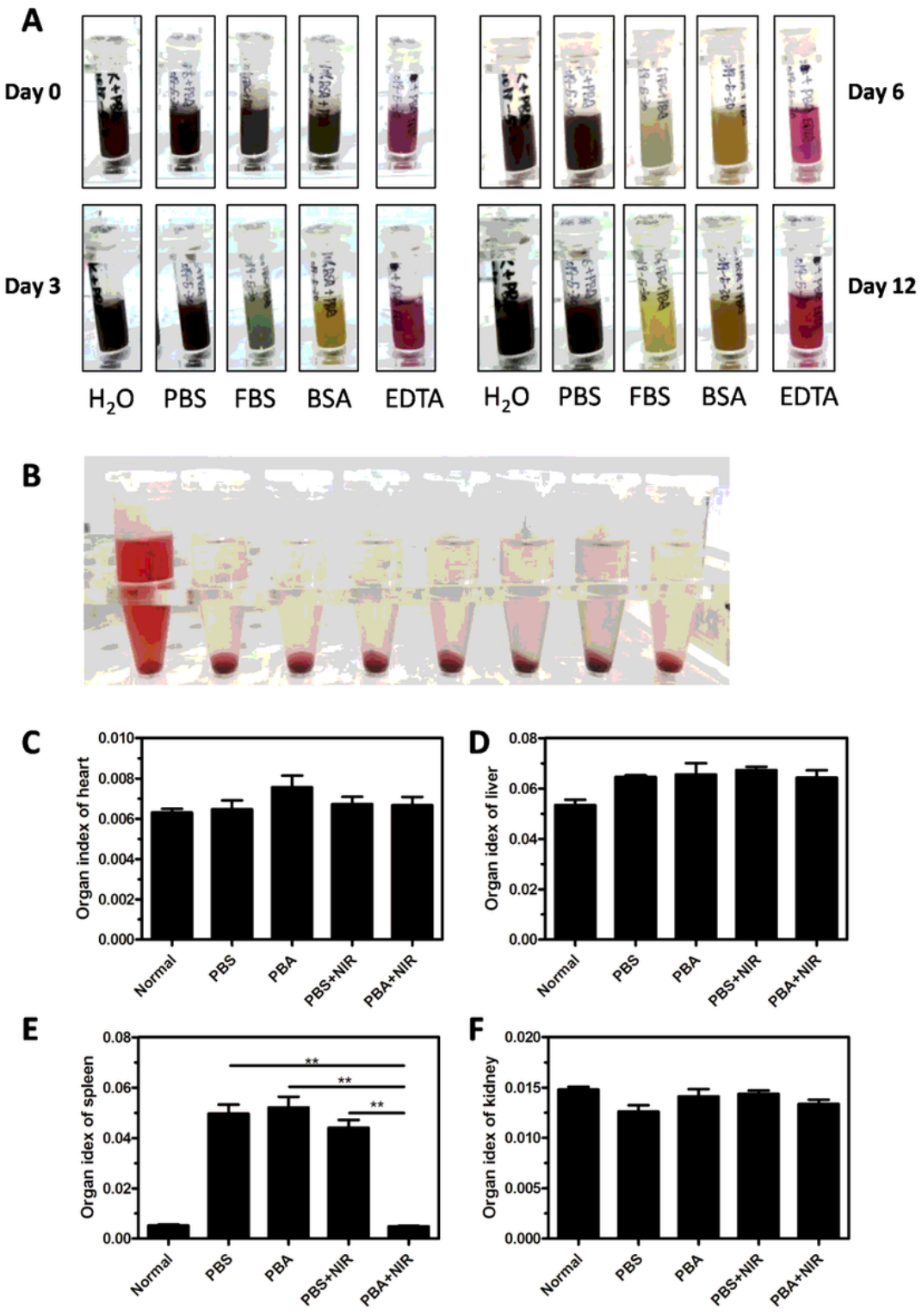

Figure 6

Biodegradability of PBA in distilled water, PBS, 10% FBS, 10% BSA and EDTA solution on day 0, day 3, day 6 and day 12 (A). Hemolysis test of different concentrations of PBA, from left to right are positive control, 31.25, 62.5, 125, 250, 500, 1000 μg mL-1 PBA and negative control group (B). The organ indexes of heart, liver, spleen and kidney in normal, PBS, PBA, PBA+NIR and PBA+NIR groups, respectively (C-F).

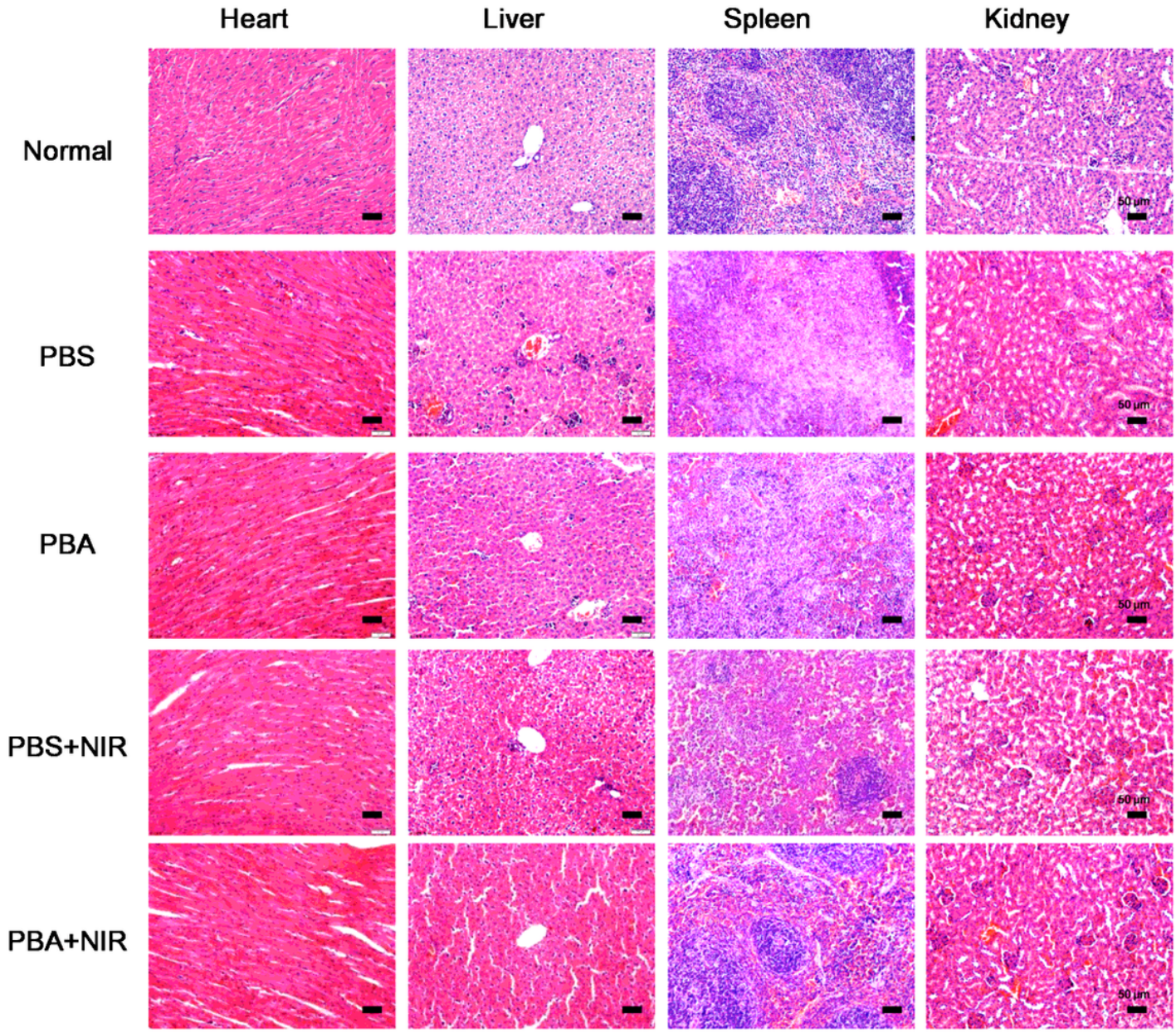

Figure 7

Histopathological study of heart, liver, spleen and kidney in normal, PBS, PBA, PBA+NIR and PBA+NIR groups, respectively.

Supplementary Files

This is a list of supplementary files associated with this preprint. Click to download.

- GraphicalAbstract.docx
- Scheme1.png